GEOPHYSICS, VOL. 67, NO. 3 (MAY-JUNE 2002); P. 872–882, 18 FIGS.
10.1190/1.1484530

Stable wide-angle Fourier finite-difference downward extrapolation of 3-D wavefields

Biondo Biondi*

ABSTRACT

I present an unconditionally stable, implicit finite-difference operator that corrects the constant-velocity phase-shift operator for lateral velocity variations. The method is based on the Fourier finite-difference (FFD) method. Contrary to previous results, my correction operator is stable even when the medium velocity has sharp discontinuities, and the reference velocity is higher than the medium velocity. The stability of the new correction enables the definition of a new downward-continuation method based on the interpolation of two wavefields: the first wavefield is obtained by applying the FFD correction starting from a reference velocity lower than the medium velocity; the second wavefield is obtained by applying the FFD correction starting from a reference velocity higher than the medium velocity. The proposed Fourier finite-difference plus interpolation (FFDPI) method combines the advantages of the FFD technique with the advantages of interpolation.

A simple and economical procedure for defining frequency-dependent interpolation weight is presented. When the interpolation step is performed using these frequency-dependent interpolation weights, it significantly reduces the residual phase error after interpolation, the frequency dispersion caused by the discretization of the Laplacian operator, and the azimuthal anisotropy caused by splitting.

Tests on zero-offset data from the SEG-EAGE salt data set show that the FFDPI method improves the imaging of a fault reflection with respect to a similar interpolation scheme that uses a split-step correction for adapting to lateral velocity variations.

INTRODUCTION

As 3-D prestack wave equation imaging becomes practically possible (Biondi and Palacharla, 1996; Mosher et al., 1997; Vaillant et al., 2000; Wyatt et al., 2000), we need robust, efficient, and accurate methods to downward continue 3-D wavefields. In particular, wide-angle methods are crucial for prestack imaging because at least one of the paths connecting the image point in the subsurface to the source–receiver locations at the surface is likely to propagate at a wide angle.

Fourier methods, such as phase shift (Gazdag, 1978), handle wide-angle propagation efficiently and accurately but only for vertically layered media. In contrast, finite-difference methods can easily handle lateral velocity variations but are not efficient for wide-angle propagation. A natural strategy thus combines a Fourier method with a finite-difference method to derive an extrapolation method that enjoys the strengths of both. This is not a new idea; indeed, the first proposed adaptations of Fourier methods, phase shift plus interpolation (PSPI) (Gazdag and Sguazzero, 1984) and split step (Stoffa et al., 1990), can be interpreted as being zero-order finite-difference corrections to a phase-shift extrapolator. Ristow and Rühl (1994) first proposed a genuine finite-difference correction to phase shift, which they dubbed Fourier finite difference (FFD). It uses implicit finite differences (Claerbout, 1985) to handle lateral velocity variations. Pseudoscreen propagators (Jin et al., 1998), wide-angle screen propagators (Xie and Wu, 1998), generalized screen propagators (Le Rousseau and de Hoop, 1998), and local Born-Fourier migration (Huang et al., 1999) are related methods that have been proposed.

The first part of this paper shows that the FFD correction is more accurate than other methods that use implicit finite difference, such as pseudoscreen propagators (Jin et al., 1998) and wide-angle screen propagators (Xie and Wu, 1998). Because the computational complexity of the three methods is comparable, the FFD correction is more attractive than the

Published on Geophysics Online January 3, 2002. Manuscript received by the Editor December 12, 2000; revised manuscript received September 19, 2001.
*Stanford University, Stanford Exploration Project, Department of Geophysics, Mitchell Building, Room 369, Stanford, California 94305-2215. E-mail: biondo@sep.stanford.edu.

others. Unfortunately, when the original FFD method is applied in the presence of sharp discontinuities in the velocity model [e.g., unsmoothed SEG/EAGE salt model (Aminzadeh et al., 1996)], it can generate numerical instability. Stability is a necessary condition for a migration method to be practically useful.

The stable FFD correction presented in this paper overcomes the instability problems related to the original FFD method. To derive a stable version of the FFD correction, I adapted the bulletproofing theory developed by Godfrey et al. (1979) and Brown (1979) for the 45° equation. The bulletproofed FFD correction is unconditionally stable for arbitrary variations in the medium velocity and in the reference velocity. Further, it is unconditionally stable when the medium velocity is either higher or lower than the reference velocity. This is a useful result and differs with a statement by Ristow and Rühl (1994) that asserts their method is unstable when the medium velocity is lower than the reference velocity. This observed instability can be explained by applying a single correction when the medium velocity is both lower and higher than the reference velocity.

The stability of the new FFD correction, even when the reference velocity is higher than the medium velocity and has lateral variations, makes it a suitable building block for constructing a new wide-angle, downward-continuation algorithm that is efficient and accurate in three dimensions. At each depth step, the wavefield is propagated with N_{v_r} reference velocities using phase shift, where N_{v_r} is determined according to both the range of velocities in the current depth slice and the maximum propagation angle needed for accurate imaging of the events of interest. Then the N_{v_r} reference wavefields are combined to create two wavefields: one for which the reference velocity is equal to or lower than the medium velocity, and the other one for which the reference velocity is equal to or higher than the medium velocity. A stable FFD correction is applied to both wavefields, and the corrected wavefields are linearly interpolated with frequency-dependent weights. The frequency-dependent interpolation significantly reduces the frequency dispersion introduced by the discretization of the Laplacian operator in the implicit finite-difference step.

In three dimensions, the FFD corrections can be applied efficiently by splitting or possibly by helix transform methods (Rickett et al., 1998). However, my proposed algorithm suffers much less from azimuthal anisotropy caused by splitting than the original FFD method. The phase errors as a function of azimuth have the opposite behavior when the differences between the reference velocity and medium velocity have opposite signs. Therefore, these phase errors tend to cancel each other when the two wavefields are interpolated after the FFD correction. Because FFD methods and interpolation are fundamental components of the new method, I refer to it as Fourier finite difference plus interpolation method (FFDPI).

The computational cost of FFDPI is obviously higher than the computational cost of simple FFD. However, FFDPI achieves higher accuracy than simple FFD. In theory, FFDPI can achieve arbitrary accuracy by using a sufficient number of reference velocities. The cost of the proposed algorithm is roughly proportional to the number of reference velocities, since its most expensive components are the fast Fourier transforms necessary to transform the wavefield between the space domain and wavenumber domain.

IMPLICIT FINITE-DIFFERENCE CORRECTION TO PHASE-SHIFT DOWNWARD CONTINUATION

Several methods have been proposed for modifying phase-shift downward continuation (Gazdag, 1978), with the goal of accommodating lateral velocity variations. Here, I analyze three methods for which the correction is applied by using an implicit finite-difference scheme: the pseudoscreen propagator (Huang et al., 1999), FFD migration (Ristow and Rühl, 1994), and the wide-angle screen propagator (Xie and Wu, 1998). All of these methods apply a correction to the wavefield after it has been downward continued using phase shift with a constant velocity. This constant velocity is often called reference velocity (v_r). The methods differ in how they approximate the difference between the one-way wave equation square root operator with the reference velocity and the same square root operator with the true medium velocity (v).

The simplest approximation is by Taylor expansion of the square root operator around v_r truncated at the first order. This approximation corresponds to the pseudoscreen propagator. It is also the basic approximation of the local Born-Fourier method (Huang et al., 1999), although in the latter migration method the correction is not applied by implicit finite difference.

The wavefield (P) downward continued at depth $z+\Delta z$ is computed from the wavefield at depth z using the following approximation:

$$P_{z+\Delta z} = P_z e^{ik_z^v \Delta z} \approx P_z e^{ik_z^{v_r} \Delta z + i\frac{dk_z}{ds}\Delta s \Delta z}, \qquad (1)$$

where the vertical wavenumber k_z^v for the medium velocity v is given, as a function of the temporal frequency ω and the horizontal wavenumber k_m, by the well-known single square root equation

$$k_z^v = \frac{\omega}{v}\sqrt{1-\frac{v^2k_m^2}{\omega^2}}. \qquad (2)$$

The first derivative of the square root, with respect to the slowness $s=1/v$ evaluated at the reference velocity v_r, is

$$\frac{dk_z}{ds} = \frac{\omega}{\sqrt{1-\frac{v_r^2k_m^2}{\omega^2}}}. \qquad (3)$$

If we use a finite difference method to apply the correction term, we need to approximate the square root in equation (3) with a rational expression. A reasonable approximation is achieved by using a Taylor expansion:

$$\frac{dk_z}{ds} \approx \omega\left[1+\frac{v_r^2X^2}{2}+\frac{3v_r^4X^4}{8}+\cdots\right], \qquad (4)$$

where $X=k_m/\omega$. When used in conjunction with an implicit finite-difference scheme, Muir's continued fraction expansion (Jacobs and Muir, 1981) is a computationally more efficient approximation than a Taylor expansion. A second-order continued fraction expansion is about as accurate as the fourth-order Taylor expansion, but it includes only second-order terms for the spatial derivatives (i.e., X^2 instead of X^2 and X^4); that is,

$$\frac{dk_z}{ds} \approx \omega \left[1 + \frac{\frac{v_r^2 X^2}{2}}{1 - \frac{3v_r^2 X^2}{4}} \right]. \qquad (5)$$

Notice that the first term of the correction in both equations (4) and (5) corresponds to the split-step correction term (Stoffa et al., 1990).

Figure 1 demonstrates the accuracy improvement gained by including the second term in equation (5). It compares the phase curves obtained after the first term in equation (5) (split step) is applied and after both terms (pseudoscreen) are applied. The medium velocity v is equal to 2 km/s, and two reference velocities are assumed: one 10% lower than the medium velocity (1.8 km/s), the other 10% higher than the medium velocity (2.2 km/s).

FFD correction

The FFD correction achieves better accuracy than the pseudoscreen correction because it is based on a direct expansion of the difference between the square root evaluated at v and the square root evaluated at v_r, instead of being based on the expansion of the square root around v_r. The downward-continued wavefield is approximated as

$$P_{z+\Delta z} = P_z e^{ik_z^v \Delta v} \approx P_z e^{ik_z^{v_r} \Delta z + i \frac{\Delta k_z}{\Delta s} \Delta s \Delta z}, \qquad (6)$$

where the Taylor series of the correction term is now

$$\frac{\Delta k_z}{\Delta s} \approx \omega \left[1 + \frac{v_r v X^2}{2} + \frac{v_r v \left(v_r^2 + v^2 + v_r v\right) X^4}{8} + \cdots \right] \qquad (7)$$

and the continued fraction approximation of the correction term is

$$\frac{\Delta k_z}{\Delta s} \approx \omega \left[1 + \frac{\frac{v_r v X^2}{2}}{1 - \frac{\left(v_r^2 + v^2 + v_r v\right) X^2}{4}} \right]. \qquad (8)$$

Both equations (7) and (8) respectively reduce to equations (4) and (5) if $v = v_r$. Therefore, at the limit when the difference between the reference velocity and the medium velocity is small, the two correction terms are equivalent, but they differ for larger corrections.

The superiority of the FFD correction is demonstrated in Figure 2. It compares the phase curves obtained after the pseudoscreen correction [equation (5)] and the FFD correction [equation (8)] were applied. As in Figure 1, the medium velocity v is equal to 2 km/s, and two reference velocities are assumed: one 10% lower than the medium velocity (1.8 km/s), and the other 10% higher than the medium velocity (2.2 km/s).

Figures 3 and 4 show the impulse responses associated with the phase curves in Figure 2. The maximum frequency in the data is 63 Hz, and the spatial sampling is 10 m horizontally and 5 m vertically. Figure 3 shows the exact impulse response for $V = 2$ km/s. Figure 4a shows the impulse response for $v_r = 1.8$ km/s and FFD correction. Figure 4b shows the impulse response for $v_r = 2.2$ km/s and FFD correction.

Notice the frequency dispersion in both the images obtained with the FFD correction. These artifacts are caused by the discretization errors of the horizontal Laplacian operator in X^2. To generate these figures, I used the classical second-order three-point approximation of the Laplacian. The phase curves shown in Figure 2 neglect this approximation; thus, they represent the effective phase shift for zero-frequency data. Also notice that the frequency dispersion is in the opposite directions

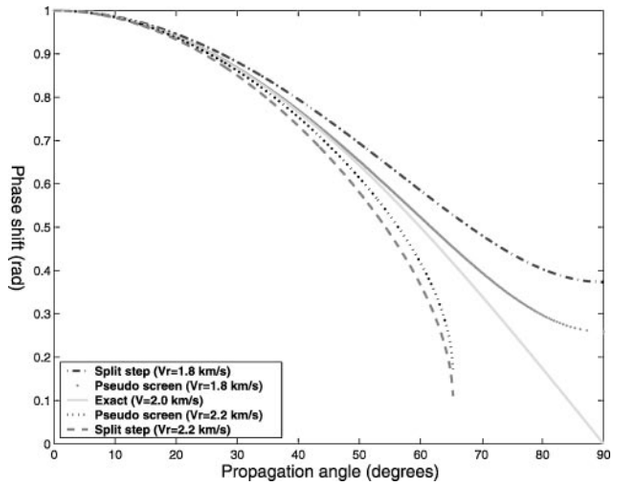

FIG. 1. Phase curves that compare the accuracy of the pseudoscreen correction with the simple split-step correction.

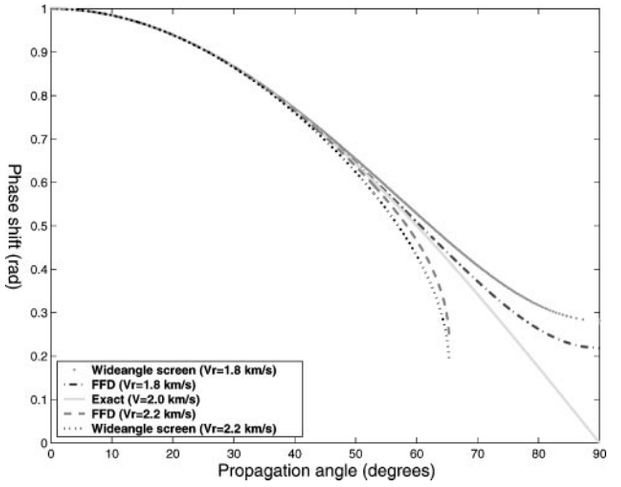

FIG. 2. Phase curves that compare the accuracy of FFD correction with the pseudoscreen correction.

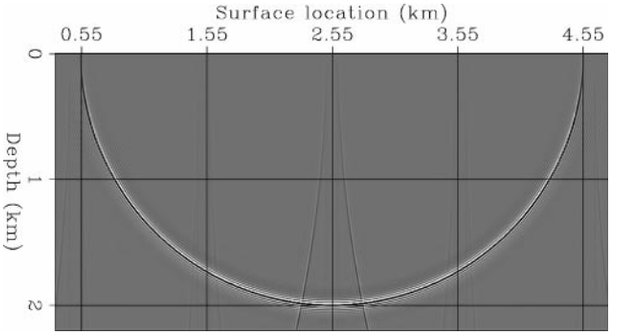

FIG. 3. Impulse response for the medium velocity equal to 2 km/s.

for opposite signs of the velocity correction. The FFDPI method exploits these opposite directions of the frequency-dispersion errors, reducing the related artifacts without additional computational complexity. Frequency-dispersion artifacts could be further reduced if the accuracy of the discrete Laplacian operator were improved—for example, by using the well-known 1/6 trick (Claerbout, 1985). Another way to reduce frequency dispersion would be to use more accurate, but also more computationally expensive, approximations of the Laplacian, such as a fourth-order five-point approximation.

Wide-angle screen correction

Wide-angle screen migration (Xie and Wu, 1998; Huang and Fehler, 2000) is similar to the methods discussed above. The continued-fraction expression for the wide-angle screen correction is

$$\frac{\widehat{\Delta k_z}}{\Delta s} \approx \omega \left[1 + \frac{\frac{v_r v X^2}{2}}{1 - \frac{\left(v_r^2 + v^2\right) X^2}{4}} \right]. \qquad (9)$$

It differs from the FFD correction in equation (8) as it misses one term ($v_r v$) in the sum at the denominator. It is not as accurate as the FFD correction, as demonstrated by Figure 5. For relatively small velocity perturbations (<15%) the wide-angle screen correction is actually less accurate than the pseudoscreen correction, as is evident by comparing Figures 5 and 2. As the velocity perturbation increases, the wide-angle screen correction becomes more accurate than the pseudoscreen correction, but it is still less accurate than the FFD correction.

The accuracy of all the corrections presented above can be improved, as discussed by Cockshott and Jakubowicz (1996), if the coefficients in the continued fraction approximation are optimized in a way similar to the optimization of the one-way equation by Lee and Suh (1985). Ristow and Rühl (1994) propose a local, and computationally intensive, method for optimizing the coefficients of the FFD correction. Huang and Fehler (2000) propose a global, and thus less computationally demanding, method for optimizing the coefficients of the wide-angle screen correction. If these optimization schemes were applied in conjunction with the FFDPI method, the accuracy of the FFDPI method would improve further. However, this paper does not discuss the optimization of the coefficients in any detail and does not use it for the numerical examples.

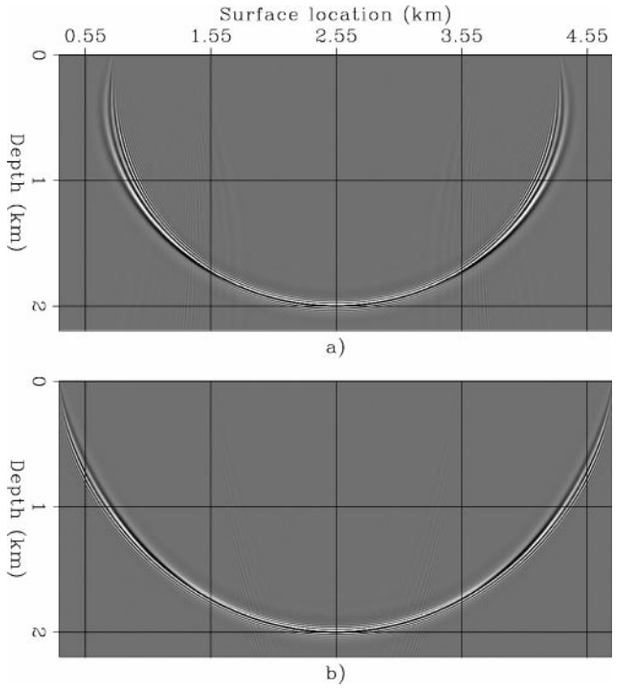

FIG. 4. Impulse responses with FFD correction and reference velocity equal to (a) 1.8 km/s and (b) 2.2 km/s.

STABLE FFD CORRECTION

An implicit finite-difference implementation using a Crank–Nicolson scheme of the FFD correction as expressed in equation (8) is stable for smooth velocity variations. But numerical instability may develop when there are sharp discontinuities in the velocity field. An example of this situation is shown in Figures 6 and 7. The slowness function (Figure 6) has a sharp negative step and a random behavior within the low-slowness region. The impulse response computed by the original FFD correction is shown in Figure 7, and it clearly illustrates the problem. Notice that the image was clipped at the 70th percentile before it was plotted so the shadow of the familiar circular impulse response could be visible in the plot.

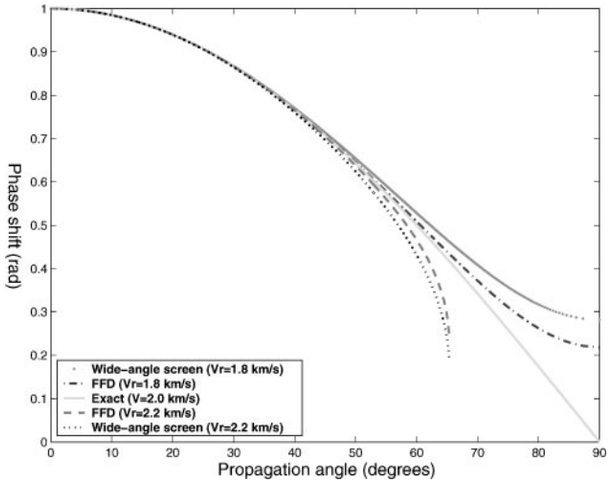

FIG. 5. Phase curves that compare the accuracy of FFD correction with the wide-angle screen correction.

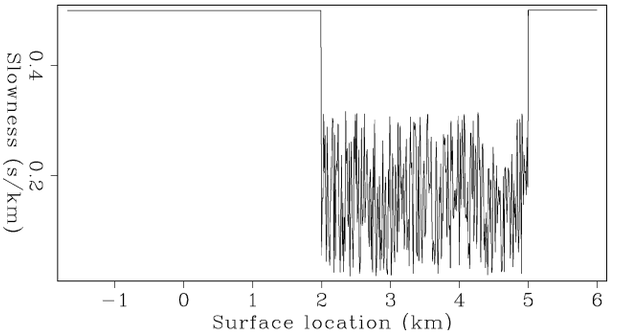

FIG. 6. Depth slice through the slowness function that causes the original FFD correction to become unstable.

In constant velocity, the correction operator is unitary (all-pass filter) because its eigenvalues have zero imaginary parts. Numerical instability originates when variations in the velocities terms multiplying the second derivative [$v_r v X^2$ and $(v_r^2+v^2+v_r v)X^2$] cause the imaginary part to become different from zero. To ensure that this does not happen, we first rewrite equation (8) as

$$\frac{\Delta k_z}{\Delta s}\Delta s \approx \omega\left\{\frac{(v_r-v)}{v_r v}+\left[\frac{2(v_r-v)}{v_r^2+v^2+v_r v}\right]\times\frac{\frac{\left(v_r^2+v^2+v_r v\right)X^2}{4}}{1-\frac{\left(v_r^2+v^2+v_r v\right)X^2}{4}}\right\}. \tag{10}$$

Then we rewrite $(v_r^2+v^2+v_r v)X^2$ as the product of a matrix with its adjoint:

$$\Sigma' X^2\Sigma = -\frac{1}{\omega^2\Delta x^2}\Sigma' D' D\Sigma = -\frac{1}{\omega^2\Delta x^2}\Sigma' T\Sigma = -\frac{1}{\omega^2\Delta x^2}\Sigma'\begin{bmatrix} 2 & -1 & 0 & \dots & 0\\ -1 & 2 & -1 & \dots & 0\\ 0 & -1 & 2 & \dots & 0\\ \vdots & \vdots & \vdots & \ddots & \vdots\\ 0 & 0 & 0 & \dots & 2\end{bmatrix}\Sigma, \tag{11}$$

where

$$\Sigma = \frac{1}{2}\,\mathrm{Diag}\begin{bmatrix}\sqrt{{}_1v^2+{}_1v_r^2+{}_1v\,{}_1v_r}\\ \vdots\\ \sqrt{{}_{i-1}v^2+{}_{i-1}v_r^2+{}_{i-1}v\,{}_{i-1}v_r}\\ \sqrt{{}_iv^2+{}_iv_r^2+{}_iv\,{}_iv_r}\\ \sqrt{{}_{i+1}v^2+{}_{i+1}v_r^2+{}_{i+1}v\,{}_{i+1}v_r}\\ \vdots\\ \sqrt{{}_nv^2+{}_nv_r^2+{}_nv_n v_r}\end{bmatrix}. \tag{12}$$

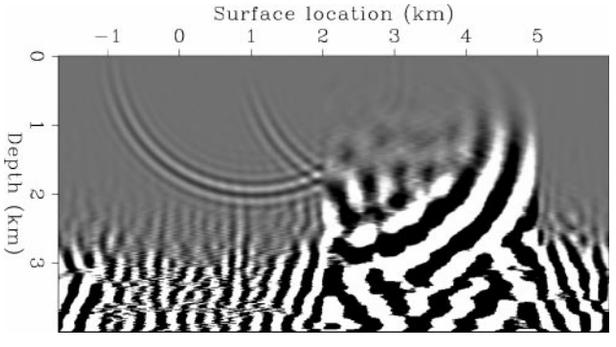

FIG. 7. Impulse response computed with the original FFD correction and assuming the slowness function shown in Figure 6. The image was clipped at the 70th percentile before it was plotted so the shadow of the familiar circular impulse response could be visible in the plot.

The values ${}_iv_r$ and ${}_iv$ are, respectively, the reference velocity and medium velocity at the i grid horizontal location.

The matrix $\Sigma' X^2\Sigma$ is now guaranteed to have real eigenvalues. Because both I and $\Sigma' X^2\Sigma$ are normal matrices that can be diagonalized by the same similarity transformation (Brown, 1979), the matrix $(I+\Sigma' X^2\Sigma)^{-1}\Sigma' X^2\Sigma$ is also guaranteed to have real eigenvalues.

In matrix notation, equation (10) can be rewritten as

$$\frac{\Delta k_z}{\Delta s}\Delta s \approx \omega\left[\frac{(v_r-v)}{v_r v}+\mathrm{sign}(v-v_r)\Delta\frac{\Sigma' X^2\Sigma}{I+\Sigma' X^2\Sigma}\right], \tag{13}$$

where

$$\Delta = 2\,\mathrm{Diag}\begin{bmatrix}\frac{|{}_1v_r-{}_1v|}{{}_1v^2+{}_1v_r^2+{}_1v\,{}_1v_r}\\ \vdots\\ \frac{|{}_{i-1}v_r-{}_{i-1}v|}{{}_{i-1}v^2+{}_{i-1}v_r^2+{}_{i-1}v\,{}_{i-1}v_r}\\ \frac{|{}_iv_r-{}_iv|}{{}_iv^2+{}_iv_r^2+{}_iv\,{}_iv_r}\\ \frac{|{}_{i+1}v_r-{}_{i+1}v|}{{}_{i+1}v^2+{}_{i+1}v_r^2+{}_{i+1}v_{i+1}v_r}\\ \vdots\\ \frac{|{}_nv_r-{}_nv|}{{}_nv^2+{}_nv_r^2+{}_nv\,{}_nv_r}\end{bmatrix}. \tag{14}$$

To perform the next, and last, step of the bulletproofing process, I pulled the sign of the velocity perturbations outside the diagonal matrix Δ. To demonstrate that multiplication by Δ does not introduce instability, I first recognize that multiplying the wavefield by the exponential of the second term in equation (13) is equivalent to solving the differential equation,

$$\frac{d}{dz}P = i\omega\,\mathrm{sign}(v-v_r)\Delta\frac{\Sigma' X^2\Sigma}{I+\Sigma' X^2\Sigma}P. \tag{15}$$

Notice that the equivalence is true only if $\mathrm{sign}(v-v_r)$ is constant, that is, if the reference velocity v_r is always lower or always higher than the medium velocity v. Second, I change variable $P=\Delta^{\frac{1}{2}}Q$, and equation (15) becomes

$$\frac{d}{dz}Q = \Delta^{\frac{1}{2}}\left(i\omega\,\mathrm{sign}(v-v_r)\frac{\Sigma' X^2\Sigma}{I+\Sigma' X^2\Sigma}\right)\Delta^{\frac{1}{2}}Q = \Delta^{\frac{1}{2}}(i\omega S)\Delta^{\frac{1}{2}}Q. \tag{16}$$

The norm $\|Q\|_{\Delta^{-1}}$ is constant with depth because the eigenvalues of S are real, and it obeys the differential equation

$$\frac{d}{dz}\|Q\|^2_{\Delta^{-1}} = Q^*(i\omega S - i\omega S^*)Q = 0. \tag{17}$$

Equation (17) guarantees the stability of the new FFD correction, independently from the value of sign $(v-v_r)$, as long the sign is constant. In theory, (v_r-v) should be never equal zero to avoid singularities in the norm $\|Q\|_{\Delta^{-1}}$. In practice, I never had to enforce this condition, although it would be easy to do so.

The reference velocity v_r and the medium velocity v can be interchanged at will in the previous development without

changing the stability conditions. Therefore, the stable FFD correction is not only stable in presence of sharp discontinuities in the medium velocity but also in the presence of sharp discontinuities in the reference velocity. This property is exploited in the next section for the design of an efficient and accurate interpolation scheme.

Equation (15) can be solved using a Crank–Nicolson scheme and the wavefield at depth $z + \Delta z$, computed as

$$P_{z+\Delta z} = \frac{1 + i\,\mathrm{sign}(v - v_r)\omega\frac{\Delta z}{2}\Delta\frac{\Sigma' X^2 \Sigma}{I + \Sigma' X^2 \Sigma}}{1 - i\,\mathrm{sign}(v - v_r)\omega\frac{\Delta z}{2}\Delta\frac{\Sigma' X^2 \Sigma}{I + \Sigma' X^2 \Sigma}} P_z. \quad (18)$$

Figure 8 shows the same impulse response as in Figure 7 but is computed by the stable FFD correction. In this case no numerical instability is encountered, and the wavefield propagates without problems through the region with random slowness perturbations.

The stable FFD correction could be also applied to downward continue a 3-D wavefield within a Crank–Nicolson solver, as summarized in equation (18). However, in three dimensions equation (18) would imply the solution of a linear system with a banded matrix with a much wider band than that in two dimensions. The cost of the exact 3-D solution would thus be considerably higher than the 2-D solution because the cost of banded-matrix solvers is proportional to the width of the band. To reduce computational cost, a splitting algorithm (Jakubowicz and Levin, 1983) can be used. The stability of a splitting algorithm is derived directly from the analysis above, since splitting consists of the successive application of the FFD correction along the two horizontal coordinate axes. In the next section I discuss how the ability to use both positive and negative velocity corrections yields a significant improvement in the accuracy of the splitting algorithm.

Boundary conditions

A necessary component of deriving a stable downward-continuation scheme is to define stable boundary conditions. It is also desirable for the boundaries to be absorbing. Following Clayton and Engquist (1980) and Rothman and Thorson (1982), this goal can be easily accomplished if the values at the edges of the diagonal of T in equation (11) are changed from 2 to $(1 + p_b)$, where $p_b = [p_r, i\,\mathrm{sign}(v - v_r)|p_i|]$, that is, substituting T with

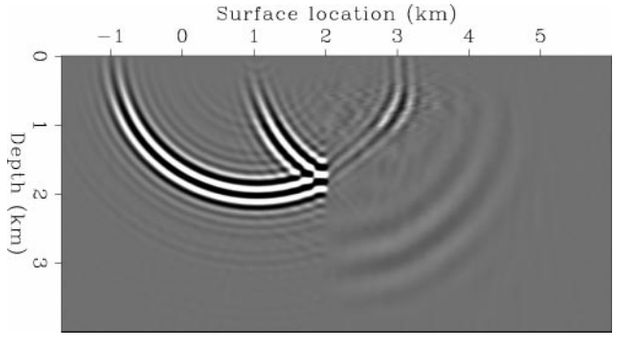

FIG. 8. Impulse response computed with the stable FFD correction and assuming the slowness function shown in Figure 6.

$$T_b = \begin{bmatrix} (1+p_b) & -1 & 0 & \dots & 0 \\ -1 & 2 & -1 & \dots & 0 \\ 0 & -1 & 2 & \dots & 0 \\ \vdots & \vdots & \vdots & \ddots & \vdots \\ 0 & 0 & 0 & \dots & (1+p_b) \end{bmatrix}. \quad (19)$$

The sign of the imaginary part of p_b determines whether the boundaries are absorbing or amplifying; therefore, the sign of $(v - v_r)$ must be constant so that instability cannot develop at the boundaries. This requirement is consistent with the stability analysis developed in equations (15)–(17). The actual values of p_r and p_i determine the propagation angle of the incident wavefield that is most strongly attenuated. In practice, to ensure both strong attenuation and weak reflection from the boundaries, I use boundary strips a few samples wide instead of a single boundary layer.

THE FFDPI ALGORITHM

The stable FFD correction has the characteristics needed for use as the main building block of an efficient and accurate wide-angle downward continuation algorithm. To achieve accuracy, we can interpolate between wavefields that have been phase shifted with several reference velocities and corrected by the stable FFD method. In theory, arbitrary accuracy can be achieved by an increase in the number of reference velocities. The structure of the algorithm is similar to the PSPI method (Gazdag and Sguazzero, 1984) and the extended split-step method (Kessinger, 1992), except that a wide-angle correction (FFD) is used instead of a narrow-angle one (vertical shift). This improvement reduces the errors over the whole range of propagation angles.

Two results reached in the previous section are important for defining a stable and accurate interpolation scheme. First, the stability of the FFD correction is independent of the sign of the velocity perturbation to be applied, as long as the sign is constant within the same correction step. This result enables a linear interpolation between a wavefield corresponding to reference velocities lower than the medium velocity and a wavefield corresponding to reference velocities higher than the medium velocity. Previously, because the reference velocity had to be lower than the medium velocity, only a nearest-neighborhood interpolation was possible when multiple velocities were used in conjunction with wide-angle corrections (Huang et al., 1999). Second, the reference velocity can vary at will laterally without compromising the stability of the method. Because of these results, it is sufficient to apply the FFD correction only twice at each depth step, minimizing computations. The first correction would be applied to a wavefield constructed from all of the reference wavefields computed with a reference velocity lower than the medium velocity. The second would be applied to a wavefield constructed from all of the reference wavefields computed with a reference velocity higher than the medium velocity.

The algorithm outlined above can be described in more detail as a sequence of steps.

First, determine a set of N_{v_r} reference velocities v_r^j as a function of the velocity range within the depth level. Gazdag and Sguazzero (1984) discuss the advantages of setting the

reference velocities to form a geometric progression. The ratio between two successive velocities depends on the maximum propagation angle required to image all of the reflectors of interest.

Second, downward continue the data and compute all the reference wavefields $P^{v_r^j}_{z+\Delta z}$ as

$$P^{v_r^j}_{z+\Delta z} = P_z e^{i k_z^{v_r^j} \Delta z} \quad \text{with} \quad j = 1, \ldots, j, \ldots, N_{v_r}. \tag{20}$$

Third, define two reference velocity functions v_r^- and v_r^+ that at every point are respectively equal to the reference velocity that is just lower and just higher than the medium velocity; that is,

$$v_r^- = \sum_{j=1}^{N_{vr}} \delta^- v_r^j \text{ where } \delta^- = \begin{cases} 1 & \text{if } v_r^j \le v < v_r^{j+1} \\ 0 & \text{elsewhere} \end{cases} \tag{21}$$

$$v_r^+ = \sum_{j=1}^{N_{vr}} \delta^+ v_r^j \text{ where } \delta^+ = \begin{cases} 1 & \text{if } v_r^{j-1} \le v < v_r^j \\ 0 & \text{elsewhere} \end{cases}. \tag{22}$$

(Figure 9 shows an example of how v_r^- and v_r^+ are defined when there are given four reference velocities and a medium velocity function v that is laterally varying and includes a fast salt layer.)

Fourth, extract two wavefields ($P^-_{z+\Delta z}$ and $P^+_{z+\Delta z}$), corresponding to v_r^+ and v_r^- and correct them by the stable FFD method:

$$P^-_{z+\Delta z} = e^{i \frac{\Delta k_z}{\Delta s} \frac{(v_r^- - v)}{v_r^- v} \Delta z} \sum_{j=1}^{N_{vr}} \delta^- P^{v_r^j}_{z+\Delta z}, \tag{23}$$

$$P^+_{z+\Delta z} = e^{i \frac{\Delta k_z}{\Delta s} \frac{(v_r^+ - v)}{v_r^+ v} \Delta z} \sum_{j=1}^{N_{vr}} \delta^+ P^{v_r^j}_{z+\Delta z}. \tag{24}$$

Finally, linearly interpolate the two corrected wavefield as

$$P_{z+\Delta z} = W^- P^-_{z+\Delta z} + W^+ P^+_{z+\Delta z}. \tag{25}$$

The interpolation weights can be chosen to zero the phase error for a given propagation angle θ_0 as follows:

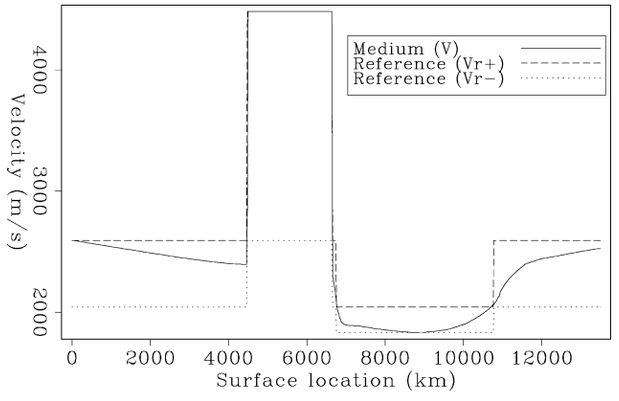

FIG. 9. Example of how the velocity functions v_r^- and v_r^+ are defined when there are four reference velocities and a medium-velocity function v that is laterally varying and includes a fast (4.5 km/s) salt layer.

$$W^- = \begin{cases} \dfrac{k_z^v - k_z^{v_r^+} - \dfrac{\Delta k_z}{\Delta s}\dfrac{(v_r^+ - v)}{v_r^+ v}}{k_z^{v_r^-} + \dfrac{\Delta k_z}{\Delta s}\dfrac{(v_r^- - v)}{v_r^- v} - k_z^{v_r^+} - \dfrac{\Delta k_z}{\Delta s}\dfrac{(v_r^+ - v)}{v_r^+ v}} & \\ & \text{if } \Im\left(k_z^{v_r^+}\right) = 0 \\ 1 & \text{elsewhere} \end{cases} \tag{26}$$

$$W^+ = 1 - W^-.$$

Notice that $W^- = 1$ where the reference wavefield becomes evanescent for the higher reference velocity (v_r^+), that is, when $\Im(k_z^{v_r^+}) \neq 0$.

The interpolation weights can be made frequency dependent to decrease the effects of frequency dispersion on the interpolated wavefield. The effective value for the horizontal wavenumber $\widehat{k_m}$ is substituted for the exact wavenumber k_m when computing $\Delta k_z / \Delta s$ in equation (27). For example, when the second derivatives are computed with the second-order approximation T_b in equation (19), $\widehat{k_m}$ is given as a function of k_m by

$$\widehat{k_m} = \frac{2}{\Delta x} \sin \frac{k_m \Delta x}{2}. \tag{27}$$

The stability analysis developed earlier applies strictly to the simple FFD correction, not to its combination with an interpolation scheme like FFDPI. In theory, when FFDPI is used, instability can still develop as it does for PSPI (Etgen, 1994; Dellinger and Etgen, 1996; Margrave and Ferguson, 1999). However, the possibility for the FFDPI algorithm to become unstable is mostly theoretical and does not represent a real practical limitation.

FFDPI error analysis

The most important advantage of the FFDPI algorithm is a drastic reduction of the propagation errors achieved when the wavefields that have been downward continued with multiple reference velocities are interpolated linearly. The errors are very small for all propagation angles up to the angle corresponding to the steepest wave that is nonevanescent with the reference velocity higher than the medium velocity (v_r^+).

This section analyzes the errors introduced by FDDPI and compares them with the errors introduced by the split-step correction used in conjunction with a wavefield interpolation scheme similar to the one described above. With a fixed number of reference velocities, the use of split-step correction instead of FFD would reduce the computational cost. To analyze the improvement in accuracy gained by the more accurate but more expensive FFD correction method, we should compare the phase errors of the two competing methods.

Figure 10 compares the relative phase errors measured as a function of the propagation angle for split step, FFD, FFDPI, and split step plus interpolation (SSPI). As in Figure 2, $v = 2$ km/s and two reference velocities were assumed: one 10% lower than the medium velocity (1.8 km/s), the other 10% higher than the medium velocity (2.2 km/s). The interpolation weights were computed by equation (27), with θ_0 set at 64°. The temporal frequency of the wavefield was assumed to be zero. The FFDPI error was contained within the ±1% band and was considerably lower than both the simple FFD and the

SSPI errors. As expected, both the FFDPI and the SSPI curves showed a zero crossing at 64°.

Because of numerical dispersion, the errors for the FFD and FFDPI methods increase as the temporal frequency of the wavefield increases. Figure 11 compares the relative phase errors measured when the temporal frequency is 100 Hz. The frequency of 100 Hz corresponds to the Nyquist wavenumber for the waves propagating at 90° with velocity of 2 km/s and

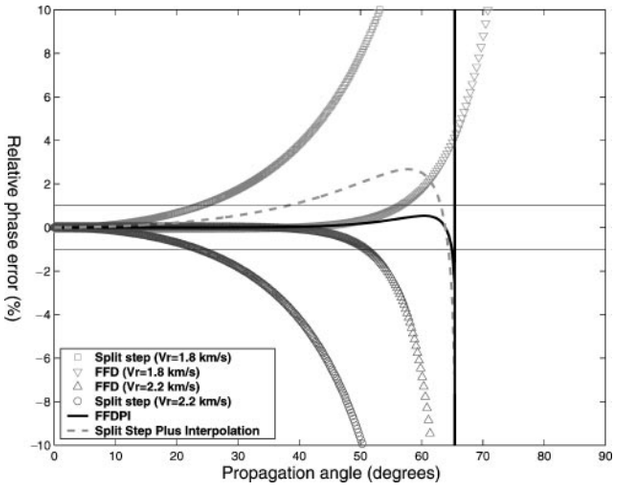

FIG. 10. Relative phase-error curves assuming $v = 2$ km/s and starting from two reference velocities ($v_r^- = 1.8$ km/s and $v_r^+ = 2.2$ km/s) for split step, FFD, FFDPI, and SSPI. The temporal frequency of the wavefield was assumed to be zero. For both FFDPI and SSPI, θ_0 was set at 64°. The vertical solid line indicates the maximum propagation angle (65.4°) when $v_r = 2.2$ km/s and $v = 2$ km/s. The horizontal solid lines indicate the 1% phase error level.

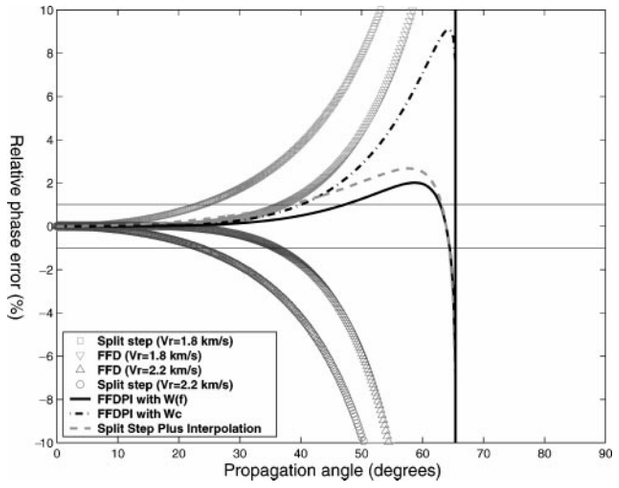

FIG. 11. Relative phase-error curves assuming $v = 2$ km/s and starting from two reference velocities ($v_r^- = 1.8$ km/s and $v_r^+ = 2.2$ km/s) for split step, FFD, FFDPI with frequency-dependent weights [FFDPI with W(f)], FFDPI with frequency-independent weights (FFDPI with Wc), and SSPI. In contrast with Figure 10, the temporal frequency of the wavefield was assumed to be 100 Hz. For both FFDPI and SSPI, θ_0 was set at 64°. The vertical solid line indicates the maximum propagation angle (65.4°) when $v_r = 2.2$ km/s and $v = 2$ km/s. The horizontal solid lines indicate the ±1% phase-error level.

spatial sampling of 10 m horizontally and 5 m vertically. Therefore, the error curves shown in Figure 11 correspond to the worst possible case for both the FFD and the FFDPI methods. There are two curves for the FFDPI method: one corresponding to frequency-independent interpolation weights, the other corresponding to frequency-dependent interpolation weights. By using frequency-dependent weights, we can greatly reduce the effects of numerical dispersion and maintain the accuracy advantages of FFDPI over SSPI. In contrast, numerical dispersion severely degrades the accuracy of the simple FFD correction at high frequency, as is evident in the impulse responses shown in Figure 4.

Figure 12 shows the impulse responses corresponding to the phase curves in Figures 10 and 11 (compare them with the impulse responses in Figures 3 and 4). The impulse response in Figure 12a was computed with frequency-independent interpolation weights. While it is much closer to the exact impulse response (Figure 3) than either of the impulse responses obtained with a simple FFD correction (Figure 4), it shows some frequency dispersion. The high frequencies are imaged inside the semicircle. The frequency dispersion is greatly reduced when the frequency-dependent interpolation weights are used, as demonstrated in Figure 12b and predicted by the curves in Figure 11.

Azimuthal anisotropy

A recurring problem that hampers the application of implicit finite-difference methods to 3-D wave extrapolation is the

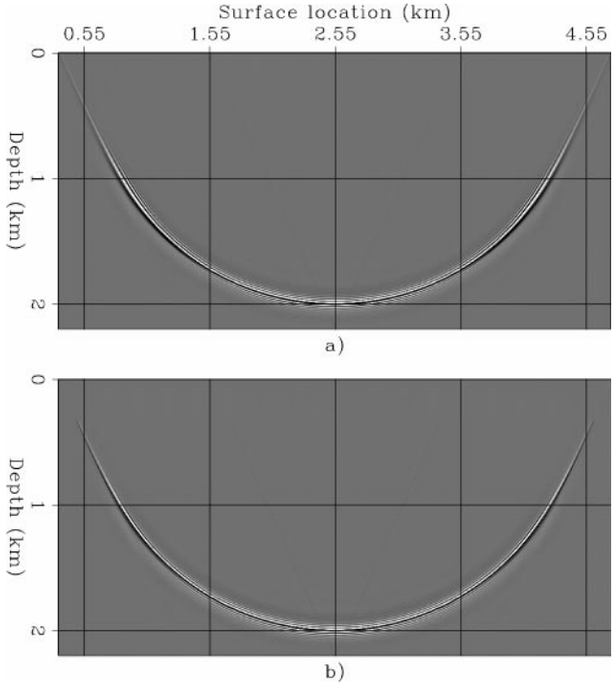

FIG. 12. Impulse responses after interpolation with (a) frequency-independent weights and (b) frequency-dependent weights. The maximum frequency in the data is 63 Hz, and the spatial sampling is 10 m horizontally and 5 m vertically. Panel (a) corresponds to the phase-error curves shown in Figure 10 (FFDPI) and Figure 11 (FFDPI with Wc). Panel (b) corresponds to the phase-error curves shown in Figure 10 (FFDPI) and Figure 11 [FFDPI with W(f)].

azimuthal anisotropy associated with splitting (Jakubowicz and Levin, 1983). Of course, this problem also affects the FFD correction applied by splitting (Cockshott and Jakubowicz, 1996). Ristow and Rühl show that multiway splitting can successfully reduce the azimuthal anisotropy for both 3-D implicit finite-difference methods (1997a) and FFD methods (1997b). Multiway splitting could easily be applied in conjunction with FFDPI to further reduce azimuthal anisotropy. Another potentially attractive way of solving this problem is to use helical boundary conditions, as discussed by Rickett et al. (1998). However, in the presence of sharp discontinuities in the velocity function, the helical solution may become unstable (Rickett, 2001).

Figure 13 compares relative phase errors as a function of the azimuth measured for a propagation angle of 61°. The frequency-dependent interpolation weights were computed to zero the phase error along an azimuthal direction oriented at 22.5° with respect to the in-line/cross-line axes and at a dip angle of 61° ($\theta_0 = 61°$). The azimuthal direction of 22.5 was chosen because it is the midpoint between the two extremes of the error curves. As in the previous figures, $v = 2$ km/s, and two reference velocities are assumed: one 10% lower than the medium velocity (1.8 km/s), the other 10% higher than the medium velocity (2.2 km/s). The plots show the phase errors at two frequencies (0 and 100 Hz) for the FFDPI algorithm, the FFD correction starting from the lower reference velocity, and the FFD correction starting from the higher reference velocity. For both of the simple FFD correction cases, the azimuthal anisotropy decreases as the frequency increases, although the average phase error increases as well. But the crucial, and useful, feature of the phase error function for the FFD corrections is that the azimuthal variations are in opposite directions when the differences between the reference velocity and medium velocity have opposite signs. Consequently, the phase error of the interpolation method is contained within the ±1% band, and it is much lower than the error of either of the simple FFD corrections. At higher frequencies (100 Hz) the impulse response of FFDPI is almost perfectly isotropic.

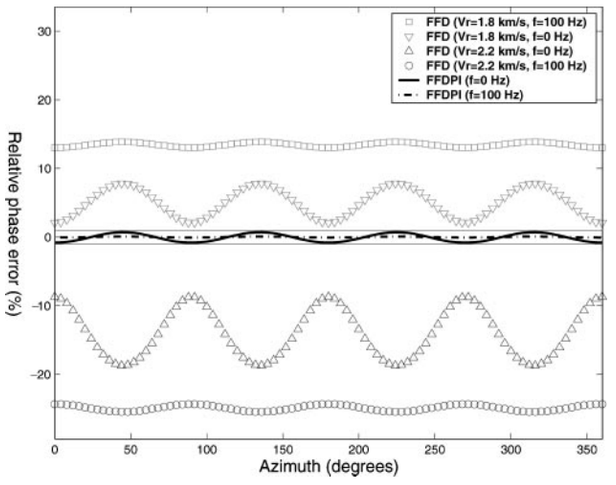

FIG. 13. Relative phase-error curves for FFD and FFDPI, as a function of the azimuth. The medium velocity was assumed to be $v = 2$ km/s, and the two reference velocities were $v_r^- = 1.8$ km/s and $v_r^+ = 2.2$ km/s. Two temporal frequencies of the wavefield were assumed: 0 and 100 Hz. The horizontal solid lines indicate the ±1% phase-error level.

The theoretical analysis is confirmed by the characteristics of the impulse responses. Figure 14 shows the depth slice of three impulse responses superimposed onto each other. The outermost circular event corresponds to the FFD correction starting from a reference velocity of 2.2 km/s. The middle event corresponds to the exact impulse response with a medium velocity of 2 km/s. The innermost event corresponds to the FFD corrections starting from a reference velocity of 1.8 km/s. The depth of the slices corresponds to a propagation angle of 64.2°, which is close to the maximum propagation angle (65.4°) for the high reference velocity (2.2 km/s). As predicted by the curves shown in Figure 13, the azimuthal anisotropy is frequency dependent, and the frequency dispersion is smaller for azimuths oriented at 45° with respect to the coordinate axes.

The comparison of Figure 15 with Figure 14 demonstrates the reduction in migration anisotropy achieved by using FFDPI in conjunction with splitting. Figure 15 is the merger of two impulse responses along the in-line direction, cut at the same depth as the slices shown in Figure 14. For negative values of the in-line coordinate, the plot shows the depth slice for the exact impulse response. For positive values of the in-line coordinate, the plot shows the depth slice for the impulse response obtained by FFDPI. It is evident that the result of the interpolation scheme is much less affected by azimuthal anisotropy and frequency dispersion than the results of the two simple FFD correction shown in Figure 14.

ZERO-OFFSET MIGRATION OF THE SEG-EAGE SALT DATA SET

To test the stability and accuracy of the FFDPI algorithm, I migrated zero-offset data from the SEG/EAGE salt data set (Aminzadeh et al., 1996). The zero-offset data were

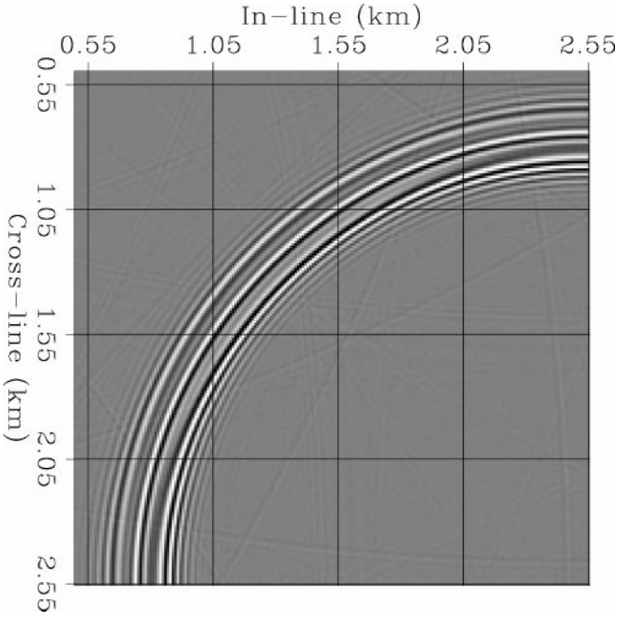

FIG. 14. Depth slices through impulse responses. Innermost event corresponds to the FFD corrections starting from a reference velocity of 1.8 km/s. Middle event corresponds to the exact impulse response with the medium velocity of 2 km/s. Outermost event corresponds to the FFD corrections starting from a reference velocity of 2.2 km/s.

obtained by stacking the near offsets (0–500 m) of the C3 Narrow Azimuth data set (Society of Exploration Geophysicists and European Association of Geoscientists and Engineers, 1997) after the data set is a good test for the stability of the FFDPI algorithm because the velocity model has sharp discontinuities caused by the salt body. Furthermore, because of a low-velocity region intended to model subsalt overpressure, several depth slices have a wide range of velocities. Figure 16 shows one of these depth slices. In the plot the salt velocity is clipped; thus, the scale bar on the side represents the range of velocities within the sediments. There is almost a factor of two between the slow-velocity sediments in the overpressure zone in the middle and the faster sediments at the edges.

To image the reflectors above the salt, the migration algorithm does not need to accurately handle lateral velocity variations, and the reflectors below the salt cannot be imaged by simple zero-offset migration. Therefore, the test focuses on a deep fault located between depths of 2 and 3 km and away from the salt body, one of the few reflectors well suited to test the accuracy of a zero-offset migration. Figure 17 shows an in-line section of the migrated cube that cuts across the fault of interest. The staircase appearance of the imaged reflectors is the result of the coarse spatial sampling of the reflectivity function used for modeling the data. Figure 17 was obtained with the FFDPI algorithm. Four reference velocities were used at each depth step. Figure 18 compares the zooms around the fault of interest. The light gray lines superimposed onto both plots

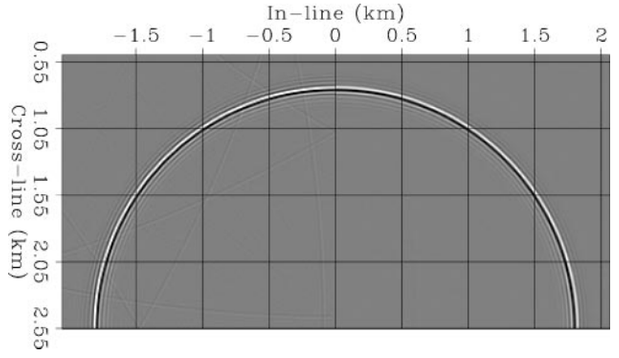

FIG. 15. Depth slices through impulse responses. Left half corresponds to the exact impulse response with the medium velocity of 2 km/s. Right half corresponds to the FFDPI results.

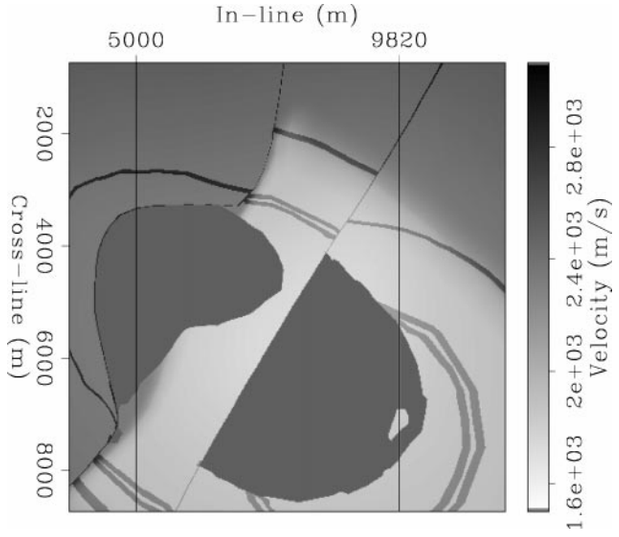

FIG. 16. Depth slice of the velocity model at depth $z = 2$ km. The salt velocity was clipped, so the scale bar on the side shows the range of velocities in the sediments.

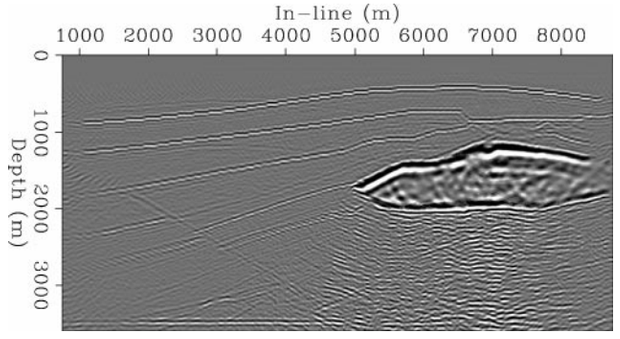

FIG. 17. In-line section of the migrated cube obtained using FFDPI.

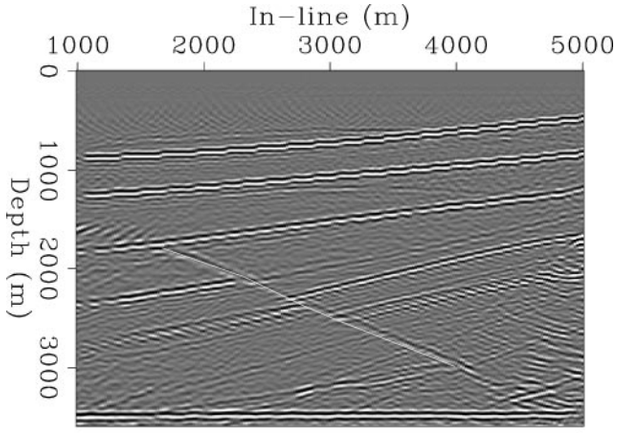

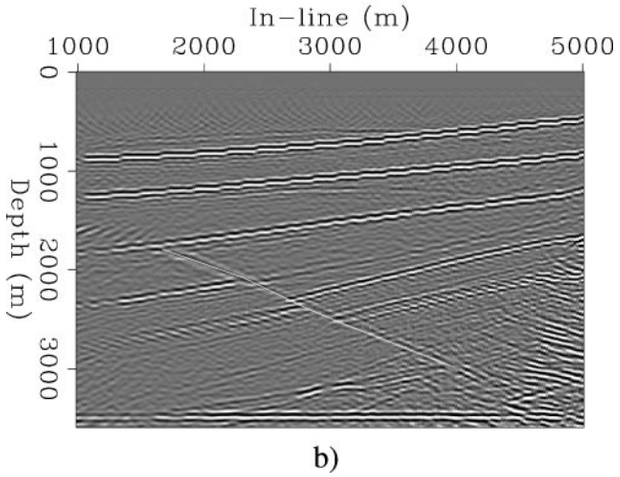

FIG. 18. Window of the same in-line section shown in Figure 17 and obtained by use of (a) split step and (b) FFDPI. The light gray lines superimposed onto the plots represent the correct fault position, as picked from the velocity model. In (a) the fault is misplaced; in (b), the fault is correctly placed.

represent the correct fault position as picked from the velocity model. Figure 18a shows the results obtained when the interpolation algorithm is used but in conjunction with the split-step correction instead of the stable FFD correction. The fault is undermigrated; thus, it is imaged too shallow and the sediment terminations are not well focused. The fault is better positioned and the image is better focused when the FFDPI algorithm is used to migrate the data (Figure 18b).

CONCLUSIONS

The combination of the Fourier method's accuracy for wide-angle propagation with the flexibility of implicit finite difference for modeling lateral velocity variations yields accurate and efficient downward propagation methods. The FFD correction is the most attractive among several methods that use implicit finite difference to correct constant-velocity phase shift for lateral velocity variations. However, the correction operator originally presented by Ristow and Rühl (1994) can be unstable in the presence of sharp discontinuities in the velocity function. I have presented and successfully tested an unconditionally stable version of the FFD correction. A simple rearrangement of coefficients is all that is necessary to make the FFD correction stable. Therefore, the stable version has computational complexity similar to that of the potentially unstable one.

Using the stable FFD correction as a building block, I derived an accurate and stable wide-angle migration (FFDPI). The FFDPI algorithm is based on the interpolation of two wavefields corrected with the FFD method, with opposite signs of the velocity perturbations. This interpolation step compensates for both the azimuthal anisotropy and the frequency dispersion of the simple FFD corrections. Therefore, the FFDPI algorithm achieves high accuracy, as demonstrated by the migration example of the SEG-EAGE salt data set.

The accuracy and cost of the FFDPI algorithm can be controlled easily by setting the number of reference velocities. Small phase errors can be achieved across the whole range of propagation angles, from zero to the limit determined by the evanescent limit for the reference velocity above the true medium velocity. The method is thus particularly attractive when high accuracy is needed for the downward-continuation operators, as in prestack depth migration below salt bodies.

ACKNOWLEDGMENTS

I thank the sponsors of the Stanford Exploration Project (SEP) for supporting the research presented in this paper. The project was also partially funded by ACTI project 4731U0015-3Q.

REFERENCES

Aminzadeh, F., Burkhard, N., Long, J., Kunz, T., and Dulcos, P., 1996, Three dimensional SEG/EAGE models—An update: The Leading Edge, **15**, 131–134.

Biondi, B., and Palacharla, G., 1996, 3-D prestack migration of common-azimuth data: Geophysics, **61**, 1822–1832.

Brown, D., 1979, Muir's rules for matrices: Another look at stability: Stanford Exploration Project Report, **20**, 125–142.

Claerbout, J. F., 1985, Imaging the earth's interior: Blackwell Scientific Publications, Inc.

Clayton, R. W., and Engquist, B., 1980, Absorbing side boundary conditions for wave equation migration: Geophysics, **45**, 895–904.

Cockshott, I., and Jakubowicz, H., 1996, 3-D migration using the Fourier finite-difference method: 66th Ann. Internat. Mtg., Soc. Expl. Geophys., Expanded Abstracts, 435–438.

Dellinger, J., and Etgen, J., 1996, Eigenvalues, singular values, and stability analysis: 66th Ann. Internat. Mtg., Soc. Expl. Geophys., Expanded Abstracts, 1975–1978.

Etgen, J. T. E., 1994, Stability of explicit depth extrapolation through laterally-varying media: 64th Ann. Internat. Mtg., Soc. Expl. Geophys., Expanded Abstracts, 1266–1269.

Gazdag, J., 1978, Wave equation migration with the phase-shift method: Geophysics, **43**, 1342–1351.

Gazdag, J., and Sguazzero, P., 1984, Migration of seismic data by phase-shift plus interpolation: Geophysics, **49**, 124–131.

Godfrey, R. J., Muir, F., and Claerbout, J. F., 1979, Stable extrapolation: Stanford Exploration Project Report, **16**, 83–87.

Huang, L. J., and Fehler, M. C., 2000, Globally optimized fourier finite-difference migration method: 70th Ann. Internat. Mtg., Soc. Expl. Geophys., Expanded Abstracts, 802–805.

Huang, L. J., Fehler, M. C., and Wu, R. S., 1999, Extended local Born Fourier migration method: Geophysics, **64**, 1524–1534.

Jacobs, B., and Muir, F., 1981, Convergence of the continued fraction for the square root function: Stanford Exploration Project Report, **26**, 183–196.

Jakubowicz, H., and Levin, S., 1983, A simple exact method of three-dimensional migration—Theory: Geophys. Prosp., **31**, 34–56.

Jin, S., Wu, R. S., and Peng, C., 1998, Prestack depth migration using a hybrid pseudo-screen propagator: 68th Ann. Internat. Mtg., Soc. Expl. Geophys., Expanded Abstracts, 1819–1822.

Kessinger, W., 1992, Extended split-step Fourier migration: 62nd Ann. Internat. Mtg., Soc. Expl. Geophys., Expanded Abstracts, 917–920.

Lee, M., and Suh, S. Y., 1985, Optimization of one-way wave equations: Geophysics, **50**, 1634–1637.

Le Rousseau, J. H., and de Hoop, M. V., 1998, Modeling and imaging with the generalized screen algorithm: 68th Ann. Internat. Mtg., Soc. Expl. Geophys., Expanded Abstracts, 1937–1940.

Margrave, G., and Ferguson, R., 1999, An explicit, symmetric wavefield extrapolator for depth migration: 69th Ann. Internat. Mtg., Soc. Expl. Geophys., Expanded Abstracts, 1461–1464.

Mosher, C. C., Foster, D. J., and Hassanzadeh, S., 1997, Common angle imaging with offset plane waves: 67th Ann. Internat. Mtg., Soc. Expl. Geophys., Expanded Abstracts, 1379–1382.

Rickett, J., 2001, Spectral factorization of wavefields and wave operators: Ph.D. thesis, Stanford University.

Rickett, J., Claerbout, J., and Fomel, S., 1998, Implicit 3-D depth migration by wavefield extrapolation with helical boundary conditions: 68th Ann. Internat. Meeting, Soc. Expl. Geophys., 1124–1127.

Ristow, D., and Rühl, T., 1994, Fourier finite-difference migration: Geophysics, **59**, 1882–1893.

——— 1997a, 3-D implicit finite-difference migration by multiway splitting: Geophysics, **62**, 554–567.

——— 1997b, Optimized operators for 3-D Fourier finite-difference migration: J. Seis. Expl. **6**, 367–383.

Rothman, D. H., and Thorson, J. R., 1982, An analysis of stable extrapolation operators with absorbing boundaries: Stanford Exploration Project Report, **32**, 105–116.

Society of Exploration Geophysicists and European Association of Geoscientists and Engineers, 1997, Salt model narrow-azimuth classic dataset (C3-NA).

Stoffa, P. L., Fokkema, J. T., de Luna Freire, R. M., and Kessinger, W. P., 1990, Split-step Fourier migration: Geophysics, **55**, 410–421.

Vaillant, L., Calandra, H., Sava, P., and Biondi, B., 2000, 3-D wave-equation imaging of a North Sea dataset: Common-azimuth migration + residual migration: 70th Ann. Internat. Mtg., Soc. Expl. Geophys., Expanded Abstracts, 874–877.

Wyatt, K. D., DeSantis, J. E., Valasek, P., Chen, T. C., Shen, Y., Meng, Z., Branham, K. L., Liu, W., Fromyr, E., and Delome, H., 2000, A 3-D wavefield imaging experiment in the deepwater Gulf of Mexico: 70th Ann. Internat. Mtg., Soc. Expl. Geophys., Expanded Abstracts, 854–857.

Xie, X. B., and Wu, R. S., 1998, Improve the wide angle accuracy of screen method under large contrast: 68th Ann. Internat. Mtg., Soc. Expl. Geophys., Expanded Abstracts, 1811–1814.